RSC Advances

PAPER

View Article Online
View Journal | View Issue

Cite this: *RSC Adv.*, 2024, **14**, 23930

Enhanced hydrogen storage property of MgH_2 caused by a $BaCrO_4$ nanocatalyst†

Chenxi Liang,[abc] Zhenbin Wang,[abc] Mingjin Zhang *[abc] and Cunhua Ma *[abc]

Magnesium hydroxide (MgH_2) has a broad application prospect in solid hydrogen storage, but the associated higher dehydrogenation temperature and undesirable cycling capacity limit its large-scale application. In this study, a $BaCrO_4$ nanocatalyst prepared *via* a wet chemistry method was added to MgH_2 to achieve better kinetic and thermodynamic performances. Kinetic tests suggested that the onset hydrogen desorption temperature was decreased for milled MgH_2 from 390 °C to below 280 °C after the introduction of a 5 wt% $BaCrO_4$ nanocatalyst and the maximum dehydrogenation amount was up to 6.32 wt%. With regard to hydrogen absorption, MgH_2 incorporated with 10 wt% $BaCrO_4$ could fully absorb 5.78 wt% H_2 within 10 min at 300 °C and recharge 3.1 wt% H_2 at a low temperature of 250 °C. In comparison, the hydrogen uptake amounts for MgH_2 under the same conditions were only 3.98 wt% and 1.52 wt%. With regard to hydrogen desorption, 5 wt% $BaCrO_4$-modified MgH_2 could discharge 4.25 wt% H_2 within 10 min at 325 °C and 4.81 wt% H_2 at 300 °C, while MgH_2 could not dehydrogenate at 300 °C. Meanwhile, only 5% of the performance decayed for 5 wt% $BaCrO_4$-modified MgH_2 during ten cycles. Dehydrogenation E_a reduced to 106.75 kJ mol^{-1} in contrast to 156.55 kJ mol^{-1} for MgH_2. In addition, DFT results verified that the $BaCrO_4$ nanocatalyst reduced the band gap from 2.78 eV to 2.16 eV to improve the thermodynamic property of MgH_2 and contributed to the decrease in the dehydrogenation energy barrier from 2.27 eV to 1.54 eV. This work provides an insight into the performance of ternary transition metal nanocatalysts for MgH_2 hydrogen storage systems.

Received 10th May 2024
Accepted 2nd July 2024

DOI: 10.1039/d4ra03460k

rsc.li/rsc-advances

1 Introduction

Since the 20th century, with the large-scale consumption of traditional fossil energy sources, which produce a large amount of greenhouse gases, researchers have conducted in-depth studies on renewable energy sources.[1–5] Regarded as one of the ideal energy carriers, hydrogen energy possesses the advantages of abundant resources, a high calorific value (33.3 kW h kg^{-1}), environment friendliness and intrinsic clean nature characteristics, which are of great significance to sustainable energy systems.[6–10] However, the key problem hindering the widespread application of hydrogen energy is the shortage of effective and secure storage systems. At present, hydrogen storage techniques mainly consist of the following categories: high-pressure gaseous state,[11] liquid state,[12] and solid state.[13] Gaseous state storage requires high pressures, and the compression process is hazardous. Liquid state storage can increase the hydrogen content to a certain extent, but energy consumption in the liquefaction process is high.[14,15] In contrast, owing to its excellent hydrogen storage performance (7.6 wt%), non-toxicity, excellent reversibility, abundant resources, and hydrogen purification function characteristics, MgH_2 is proven as an excellent system in the solid hydrogen storage field.[16–18] Nevertheless, the stable thermodynamic and sluggish kinetic properties limit the large-scale applications of MgH_2 to some extent.[19–21] In order to overcome these challenges, nanosizing,[22–25] alloying,[26–29] and catalyst doping[30–33] have been specifically studied.

Alloying improves kinetic/thermodynamic properties by changing the reaction path. However, the lower hydrogen storage density of Mg-based alloys needs to be improved further. Nanosizing could reduce the grain size and shorten the diffusion path length to improve the hydrogen storage performance of MgH_2. High-energy ball milling (HEBM) is the most commonly used method for nanotization. Schulz *et al.*[34] prepared MgH_2 nanoparticles with high specific surface area by HEBM, which could adsorb 7 wt% H_2 at 300 °C and desorb completely at 350 °C. Varin *et al.*[35] prepared MgH_2 with different particle sizes and found that when the particle size was reduced to 600 nm, the dehydrogenation temperature was reduced by

[a]*School of Chemistry and Chemical Engineering, Qinghai Normal University, Xining 810008, China. E-mail: zhangmingjin@qhnu.edu.cn; 20211001@qhnu.edu.cn; Tel: +86-971-5213524*

[b]*Academy of Plateau Science and Sustainability, People's Government of Qinghai Province & Beijing Normal University, Xining, 810016, China*

[c]*Qinghai Provincial Key Laboratory of Advanced Technology and Application of Environment Functional Materials, Xining 810008, China*

† Electronic supplementary information (ESI) available. See DOI: https://doi.org/10.1039/d4ra03460k

60 °C. However, HEBM will lead to agglomeration and growth, reducing the cycling stability of the material.

The combination of nanosizing with transition metal catalyst doping is an approach that takes into account both kinetic and cycling properties. The corresponding interaction force between the d electrons of the metal catalysts and the electrons in the H_2/H orbital can dramatically cut down the dehydrogenation E_a of MgH_2. After ball milling, the catalyst coated on the surface of MgH_2 can inhibit the agglomeration of MgH_2 and achieve ideal cycling performance.[36–38] Wang *et al.*[39] prepared a highly refined cadmium-based catalyst on nitrogen-doped carbon (Cr–N–C) and added it to MgH_2 *via* HEBM. Theoretical calculations showed that the dehydrogenation E_a of MgH_2 was reduced from 156.5 kJ mol^{-1} to 133 kJ mol^{-1}, and the hydrogen storage account did not decay after cycling (volume retention rate is 95%). The Cr element could interact strongly with H and destabilize the interaction of the Mg–H bond. Kurdyumov *et al.*[40] fabricated a MgH_2-MIL-101 (Cr) compound system through milling technology, and the results indicated that chromium oxide particles and MIL-101 (Cr) were dispersed uniformly on the surface of MgH_2. The compound system could discharge 5.0 wt% H_2 within 3000 s at 255 °C and recharge 4.8 wt% within 2000 s at 320 °C, while MgH_2 did not hydrogenate and dehydrogenate. It was obvious that Cr-based catalysts could dramatically ameliorate the kinetic capacity of MgH_2.

Compared with single-metal catalysts, multiple metal oxides have higher brittleness, which are more easily dispersed in a MgH_2 matrix by ball milling technology. Sazelee *et al.*[41] prepared MgH_2 doped with $BaFe_{12}O_{19}$, which could start dehydrogenization at 270 °C compared to MgH_2 (418 °C). No obvious capacity decay phenomenon occurred during cycling. MgO-, Fe- and Ba-based substances achieved heterogeneous catalytic effects on MgH_2, thereby ameliorating the hydrogen storage performance. Chen *et al.*[42] prepared $BaTiO_3$ to catalytically modify MgH_2, and MgH_2-20 wt% $BaTiO_3$ could fully discharge 6.0 wt% H_2 within 20 min at 310 °C. the E_a value of the composite decreased to 60 kJ mol^{-1} in contrast to that of pure MgH_2 (101 kJ mol^{-1}). It is worth noting that MgH_2-20 wt% $BaTiO_3$ could absorb 3.5 and 4.0 wt% H_2 in 120 minutes at 50 °C and 100 °C, respectively, whereas milled MgH_2 only absorbed ~1.0 wt% H_2. Ismail *et al.*[43] fabricated MgH_2-10 wt% $BaMnO_3$. Benefiting from the strong electron-withdrawing effect of O, as well as the kinetic modulation of Ba or Ba-based substances, the T_{onset} value of MgH_2-10 wt% $BaMnO_3$ reduced from 343 °C to 282 °C, with an ideal hydrogen absorption content of 5.22 wt% at 250 °C and a hydrogen desorption content of 5.36 wt% at 300 °C. Without doubt, ternary transition metal oxides, particularly Ba-based oxides, have exhibited generally distinguished catalytic effect on MgH_2.

In view of the ideal catalytic effect of Cr-based catalysts/Ba-based transition metal catalysts and the high-energy ball milling nanotization method, we successfully synthesized a $BaCrO_4$ nanocatalyst through wet chemical technology to reveal the catalytic effect on MgH_2. Up to now, there are no relevant research studies on the introduction of the $BaCrO_4$ catalyst into MgH_2 to improve the hydrogen storage performance. We focused on investigating the dynamic and thermodynamic performances of MgH_2-*x* wt% $BaCrO_4$ (x = 5, 10, and 15) through a series of kinetic test and theoretical calculation. Meantime, the structural evolution and catalytic mechanism were explored deeply.

2 Experimental details

2.1 Synthesis of $BaCrO_4$ nanocatalysts

A $BaCrO_4$ nanocatalyst was fabricated through the wet chemical technology. In detail, 0.174 g dodecylbenzene sulfonic acid sodium salt (DBSS) and 0.88 g Na_2CrO_4 (AR, 98%, Sigma-Aldrich) were dissolved in 100 mL of distilled water in a beaker. After that, vigorous stirring was carried out for two hours at room temperature to ensure that all the reagents were evenly dispersed in the solution. Then 20 mL 0.1875 mol L^{-1} $Ba(NO_3)_2$ (AR, 99%, Sigma-Aldrich) was added dropwise to the above solution for 10 min at room temperature under magnetic stirring. Yellow precipitates were produced during the addition process. After finishing the addition process, the mixture was deposited *via* continuous stirring for another 30 min, which was conducive to the formation of $BaCrO_4$ nanocrystals. Finally, precipitates were washed three times with distilled water and absolute ethanol to remove the remaining DBSS and dried at 150 °C for 2 h in a vacuum oven. The detailed procedure is shown in Fig. S1(a).†

2.2 Preparation of MgH_2-*x* wt% $BaCrO_4$ compounds

The MgH_2 (AR, 98%, Langfang Beida Trading Co., Ltd)-*x* wt% $BaCrO_4$ (x = 5, 10, and 15) compound system were prepared *via* ball milling technology under vacuum in planetary ball milling equipment (JX-4GL, Shanghai Jingxin). Each sample was milled for 4 h (ball milling for 25 minutes and rest for 5 minutes in different directions to prevent the ball mill tank from overheating) at a speed of 400 rpm. The ratio of ball to powder was 40/1. To prevent oxidation, the loading and sampling processes were carried out in a glove box filled with 5 bar argon gas and a water oxygen content less than 0.1 ppm.

3 Characterization

An X-ray diffractometer (XRD, Brucker D8 ADVACE A25) with Cu Kα radiation was used to detect the phase evolution with 2θ ranging from 10–80° at a step of 10° min^{-1}. The microstructures and element distributions were researched through Scanning electron microscopy (SEM, JEOL JSM-6610LV) and transmission electron microscopy (TEM, JEOL JEM-2100F) with an energy-dispersive spectroscopy (EDS).

A differential scanning calorimetry (DSC, NETZSCH STA449F3) instrument was used at different heating rates (5, 8, 10, and 12 °C min^{-1}) to analyze the dehydrogenation capacity. The hydrogenation kinetics was studied using a high-pressure gas absorption instrument (BSD 3H-2000 PH) at different temperatures under 3.3 MPa hydrogen pressure, and the dehydrogenation kinetics was studied under 0.001 MPa hydrogen pressure. The temperature-programmed desorption

(TPD) test was applied with a temperature range from 20 °C to 500 °C at a speed of 5 °C min^{-1}.

4 Computational details

The density functional theory (DFT) calculations were performed using the CASTEP package with the Perdew–Burke–Ernzerhof (PBE) generalized gradient approximation (GGA) exchange–correlation functional. Interactions between core and valence electrons were described using Vanderbilt ultra-soft pseudopotentials. The energy cut-off for the plane-wave basis set was 400 eV.

The threshold values of the convergence criteria are specified as follows: 0.002 Å for maximum displacement, 0.05 eV $Å^{-1}$ for maximum force, 0.1 GPa for maximum stress, 10–5 eV per atom for energy, and 2.0×10^{-6} eV per atom for self-consistent field tolerance. The 1.5 Å thickness of the MgH_2(101) surface was cleaved with $a = 25.8$ Å and $b = 8.16$ Å. A 15 Å vacuum space was implemented into the model to eliminate undesirable interactions between the bottom side of the slab and the molecules in the vacuum space. The (4 × 2) unit cell of MgH_2 (101)–$BaCrO_4$ (203) was used to inhibit the lateral interactions between the molecules on the surface.

The charge density difference of MgH_2-10 wt% $BaCrO_4$ was calculated, which is defined as $\Delta\rho = \rho_{tot} - \rho_{substrate} - \rho_{cluster}$, where ρ_{tot}, $\rho_{substrate}$, and $\rho_{cluster}$ are the total charge densities of the MgH_2-10 wt% $BaCrO_4$ compound, the MgH_2 substrate, and the $BaCrO_4$ catalyst, respectively.

When the optimization was completed, the density difference calculations were performed. Moreover, the diffusion barrier energy was located utilizing the well-known linear synchronous transit (LST) and quadratic synchronous transit (QST) methods.

5 Results and discussion

5.1 Characterization of $BaCrO_4$ nanocatalysts

Fig. S1(b)† exhibits the XRD patterns of the $BaCrO_4$ catalyst. Obviously, the diffraction peaks coincide with the standard card (JCPDS No. 78-1401), with no detection of impurity peaks. Fig. S1(c and d)† present the morphology and particle size distribution of the $BaCrO_4$ nanocatalyst. Obviously, the $BaCrO_4$ nanocatalyst exists in a relatively nano-blocky structure with a particle size ranging from 100 to 500 nm with an average size of 225 ± 17.68 nm. The micronano structure and composition of the nanocatalyst were further determined through the TEM images shown in Fig. S1(e and f).† The nano-blocky morphology can be seen in Fig. S1(e).† Meantime, the high-resolution transmission electron microscopic (HRTEM) images shown in Fig. S1(f)† detect interplanar crystal spacings of 0.399, 0.352, and 0.275 nm, corresponding to the (111), (210), and (200) planes of the $BaCrO_4$ crystal respectively, which confirms the XRD pattern above. The diffraction rings observed in the SAED image correspond to the (111), (210), and (200) planes of $BaCrO_4$ (Fig. S1(g)†). Further, the EDS test of $BaCrO_4$ indicates the uniform distribution of Ba, Cr and O (Fig. S1(h–k)),† and the elemental composition is shown in Fig. S2.†

5.2 Hydrogen storage property of MgH_2–$BaCrO_4$

MgH_2 with different contents of $BaCrO_4$ samples was fabricated to investigate the catalytic action of $BaCrO_4$ on MgH_2. The TPD test shown in Fig. 1(a and b) reveals the occurrence of the hydrogenation desorption process for the four groups of MgH_2-x wt% $BaCrO_4$ ($x = 5$, 10, and 15) samples at 390, 310, 280, and 275 °C, which have total hydrogen contents of 6.80, 6.77, 6.32 and 5.74 wt%. The onset dehydrogenation temperature and the maximum dehydrogenation amount continue to decrease with the increase in $BaCrO_4$ nanocatalyst. It is obvious that the excellent T_{onset} and higher hydrogen storage capacity are taken into account for the MgH_2-10 wt% $BaCrO_4$ sample. The T_{onset} value of MgH_2-10 wt% $BaCrO_4$ is 110 °C lower than that of milled MgH_2. In comparison to milled MgH_2 (6.80 wt%), the hydrogen storage content of the MgH_2-10 wt% $BaCrO_4$ sample is 6.32 wt%, which is attenuated to some extent, but it still meets the practical application standard. The lower T_{onset} value of MgH_2-10 wt% $BaCrO_4$ remarkably exceeds those of other catalyst-MgH_2 systems, which are reported in Fig. 1(c).[44–51]

Based on the above-mentioned conclusions, we selected 10 wt% $BaCrO_4$-modified MgH_2 for an in-depth study. The hydrogenation recharge and discharge kinetic tests were carried out at different temperatures. Fig. 2(a) depicts that milled MgH_2 absorbs 1.22, 3.15, 5.38 and 6.35 wt% H_2 at 250, 275, 300 and 350 °C within 60 min, respectively. Fig. 2(c) presents the kinetics of 10 wt% $BaCrO_4$-modified MgH_2. It is proposed that a complete hydrogen uptake of 5.78 wt% H_2 is achieved within 10 min at 300 °C. Additionally, 3.09 and 4.30 wt% of H_2 are absorbed from 10 wt% $BaCrO_4$-modified MgH_2 at 250 and 275 °C within 60 min. The considerable hydrogen storage performance is in sharp contrast to milled MgH_2, which indicates that the $BaCrO_4$ nanocatalyst exhibits excellent catalytic effects at low temperatures.

To understand the kinetics of the dehydrogenation process, Fig. 2(b and d) illustrate the hydrogen discharge curves of MgH_2 and 10 wt% $BaCrO_4$-modified MgH_2. The desorption content of milled MgH_2 is only 0.11 wt% in 60 min at 300 °C. While 10 wt% $BaCrO_4$-modified MgH_2 could desorb 4.50 wt% H_2 under the same operating conditions, and the rate of dehydrogenation is remarkably faster than that of milled MgH_2. Meantime, 10 wt% $BaCrO_4$-modified MgH_2 achieves complete dehydrogenation capacities of 5.03 wt% and 5.53 wt% within 40 min at 325 and 350 °C. In contrast, only 3.76 wt% H_2 and 4.38 wt% H_2 are released within 40 min at 350 and 375 °C for milled MgH_2. To sum up, it is obviously observed that after the incorporation of 10 wt% $BaCrO_4$ nanocatalyst, the hydrogen recharge and discharge kinetic performances of MgH_2 has been strikingly promoted.

Moreover, the long-term stable cycle dynamic capacity is an important parameter that inhibits the application of hydrogen storage materials. Therefore, the ten-cycle performance was studied, as shown in Fig. 2(e and f). The 10 wt% $BaCrO_4$-

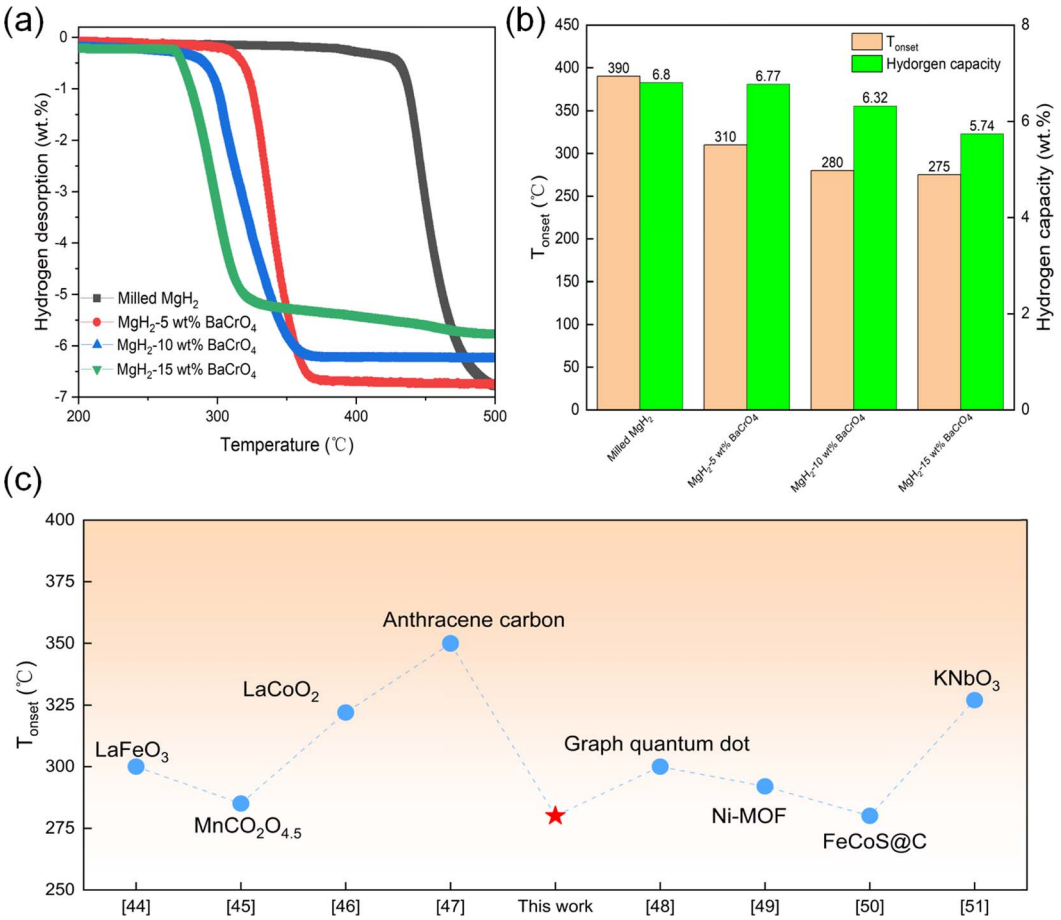

Fig. 1 (a) TPD curves and (b) several performance factors of milled MgH_2 and MgH_2-x wt% (x = 5, 10, and 15) $BaCrO_4$ systems. (c) Comparison of the onset desorption temperature of MgH_2-10 wt% $BaCrO_4$ with other catalyst-MgH_2 systems.

modified MgH_2 sample has a hydrogen storage content of 6.47 wt% and desorption content of 5.66 wt% in the first cycle, during the second to tenth cycle, the amounts of hydrogenation and dehydrogenation is maintained at approximately 5.95 wt% and 5.2 wt%, and the volume retention rate is as high as 95%, which exhibits excellent cycling dynamic performances. Meanwhile, the SEM morphology and particle size distribution shown in Fig. S3(a)† manifest that the average size decreases from 225 ± 17.68 nm of $BaCrO_4$ to 125 ± 6.23 nm after ball milling treatment, which has an excellent nano-refinement effect. Additionally, as shown in Fig. S3(b),† with an average size of 175 ± 8.52 nm, 10 wt% $BaCrO_4$-modified MgH_2 does not show obvious agglomeration after 10 cycles. This fine particle size provides a lot of diffusion channels and reaction sites for H_2 recharge and H discharge processes, which contribute to ameliorate the hydrogen storage property and achieve ideal cycling stability.

Fig. 3(a and c) show the DSC curves of milled MgH_2 and 10 wt% $BaCrO_4$-modified MgH_2 to further study the dehydrogenation kinetic property. The peak hydrogen desorption temperatures of milled MgH_2 at heating rates of 5, 8, 10 and 12 °C min^{-1} are 390, 394, 399 and 410 °C. While the peak hydrogen desorption temperatures of 10 wt% $BaCrO_4$-modified MgH_2 are 343, 355, 360 and 368 °C at the same rates. It is proposed that the peak hydrogenation desorption temperature increases with the increase in heating rate. Furthermore, it is obvious that the peak temperature decreases after the introduction of the $BaCrO_4$ nanocatalyst. This ameliorative capacity is related to the E_a value of MgH_2. Combined with the heating rate peak temperature, we used the Kissinger equation to calculate the dehydrogenation E_a value of the MgH_2–$BaCrO_4$ compound system and MgH_2 to explore the kinetics in depth. The detailed equation is expressed as follows:[52]

$$\ln(\beta/T_p^2) = -E_a/RT_p + A \quad (1)$$

where β represents the heating rate, T_p represents the peak hydrogen desorption temperature, E_a represents the activation energy barrier, R represents the gas constant and A represents the linear constant. Fig. 3(b and d) illustrate the E_a value of milled MgH_2 calculated to be 156.55 kJ mol^{-1}, while that of the MgH_2–$BaCrO_4$ system is only 106.75 kJ mol^{-1}. It is suggested that the catalyst of $BaCrO_4$ realizes a reduction in dehydrogenation E_a and improves the dynamics of MgH_2. Notably, 10 wt% $BaCrO_4$-modified MgH_2 exhibits a lower hydrogenation desorption activation energy than that of MgH_2 added with other catalysts, as shown in Table 1.

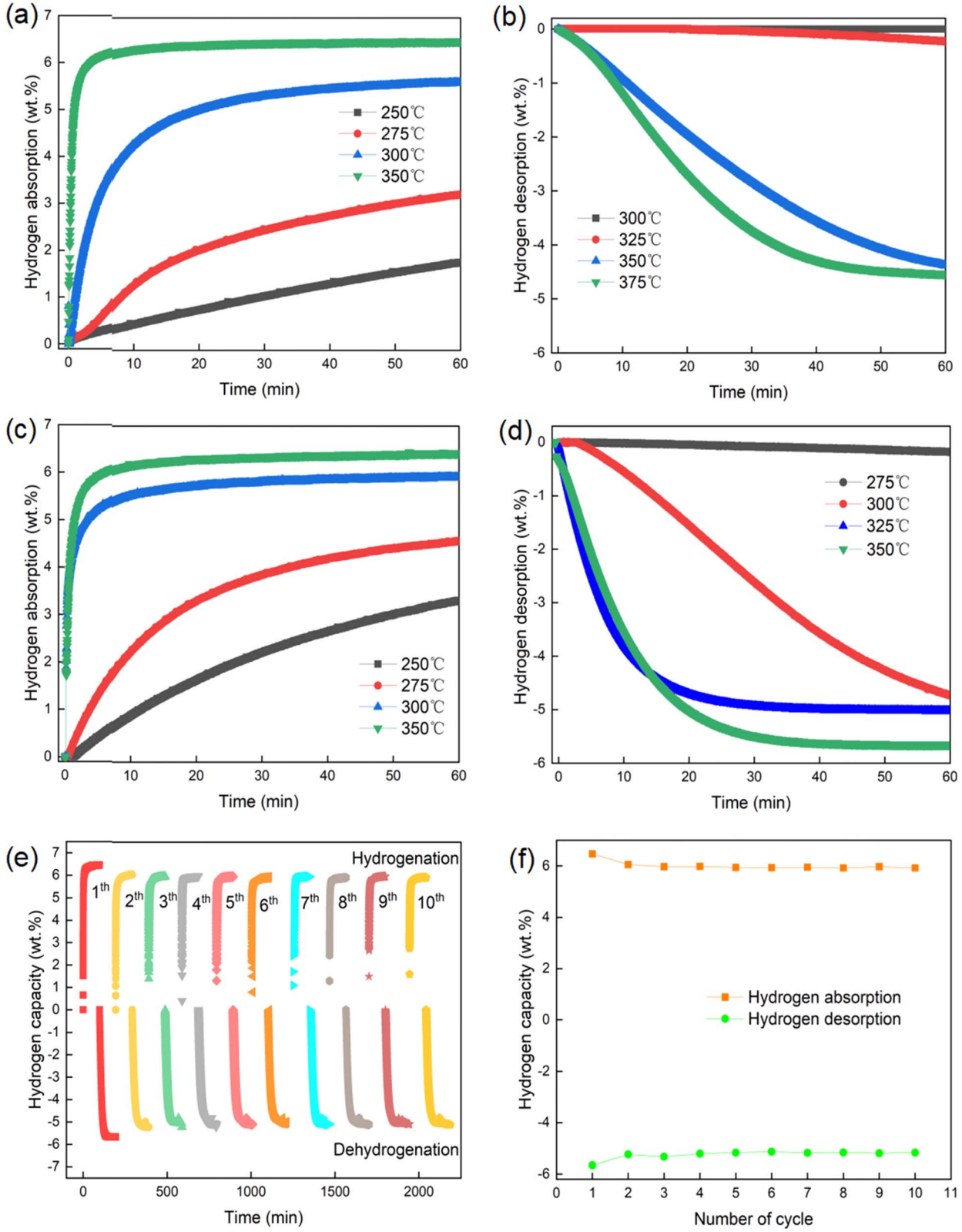

Fig. 2 (a) Hydrogen release curves of milled MgH_2 and (c) 10 wt% $BaCrO_4$-modified MgH_2. (b) Hydrogen uptake curves of milled MgH_2 and (d) 10 wt% $BaCrO_4$-modified MgH_2. (e) De/hydrogenation cycle curves and (f) decay curves of 10 wt% $BaCrO_4$-modified MgH_2.

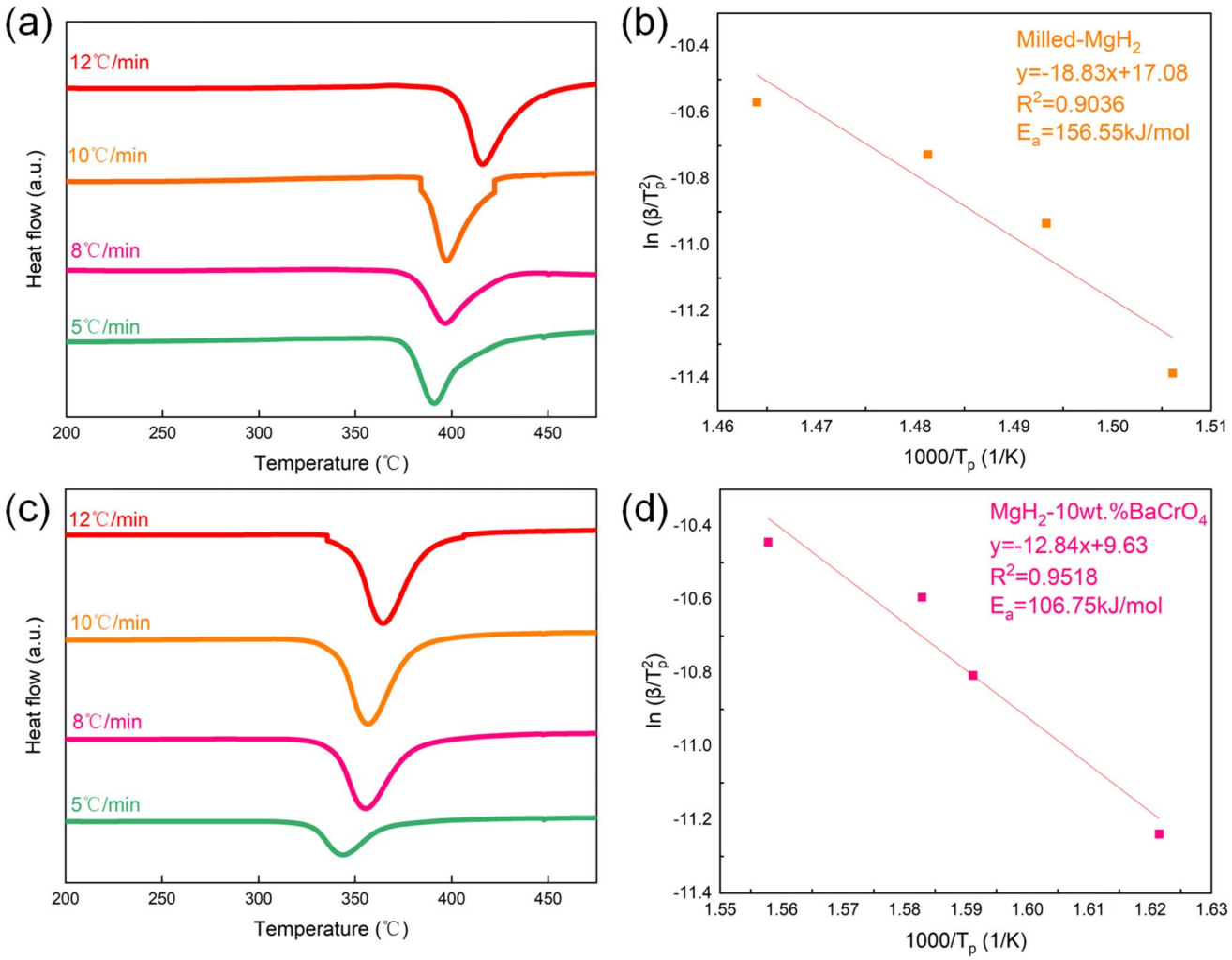

Fig. 3 (a) DSC profiles of milled MgH_2 and (c) 10 wt% $BaCrO_4$-modified MgH_2. (b) Kissinger plots of milled MgH_2 and (d) 10 wt% $BaCrO_4$-modified MgH_2.

Table 1 Hydrogen desorption activation energies of MgH_2/Mg compound systems reported in recent years

Compound	E_a (kJ mol^{-1})	Ref.
MgH_2–$LaFeO_3$	107.00	44
MgH_2–$BaFe_{12}O_{16}$	115.00	41
MgH_2–$MnFe_2O_4$	108.40	53
MgH_2–$K_2Ti_8O_{17}$	116.00	54
MgH_2–Sc_2TiO_3	109.00	55
MgH_2–MoO_3	114.70	56
MgH_2–Na_3AlF_6	129.00	57
MgH_2–Zn_2TiO_4	105.50	58
MgH_2–$BaCrO_4$	106.75	This work

5.3 Rate-controlling step kinetic model of dehydrogenation

Aiming to further analyze the kinetic behavior of hydrogen desorption, we employed the approach proposed by Sharp and Jones to explore the possible models of rate-controlling step kinetics.[59,60] Table 2 presents the specific description of some common kinetic models, which include diffusion control, geometric contraction, nucleation at growth and first-order reaction model. The specific kinetic expression is as follows:

$$d_a/d_t = kf(\alpha) \quad (2)$$

where k is a reaction rate constant, α represents the reaction extent and $f(\alpha)$ is a function depending on the reaction mechanism. $f(\alpha)$ could be represented using the following formula:

$$f(\alpha) = A(t/t_{0.5}) \quad (3)$$

where A represents the constant in connection with the kinetic model and $t_{0.5}$ represents the time when α achieves 0.5. The model with the fitting slope closest to 1 is the most suited kinetic model. Fig. 4(a) displays the hydrogen desorption curve at 350 °C for various kinetic models. It is proposed that the slope of the R3 model (0.937) is closest to 1.0. Moreover, Fig. 4(b) displays $g(\alpha)$ at different temperatures. It is worth noting that the linear fitting constants are 0.9716, 0.9930, which

Table 2 Common theoretical kinetic models for desorption curve analysis

Symbol	$g(\alpha)$	Mechanisms	Sharp's equation
D1	α^2	One-dimensional diffusion	$0.2500(t/t_{0.5})$
D2	$\alpha + (1-\alpha)\ln(1-\alpha)$	Two-dimensional diffusion	$0.1534(t/t_{0.5})$
D3	$[1-(1-\alpha)^{1/3}]^2$	Three-dimensional diffusion (Jander equation)	$0.0426(t/t_{0.5})$
D4	$1-(2\alpha/3)-(1-\alpha)^{2/3}$	Three-dimensional diffusion (Ginstling-Brounstein equation)	$0.0367(t/t_{0.5})$
F1	$-\ln(1-\alpha)$	First-order reaction	$-0.6931(t/t_{0.5})$
R2	$1-(1-\alpha)^{1/2}$	Two-dimension phase boundary (contracting area)	$0.2929(t/t_{0.5})$
R3	$1-(1-\alpha)^{1/3}$	Three-dimension phase boundary (contracting volume)	$0.2063(t/t_{0.5})$
A2	$[-\ln(1-\alpha)]^{1/2}$	Avrami eqn (1)	$0.8326(t/t_{0.5})$
A3	$[-\ln(1-\alpha)]^{1/3}$	Avrami eqn (2)	$0.8850(t/t_{0.5})$

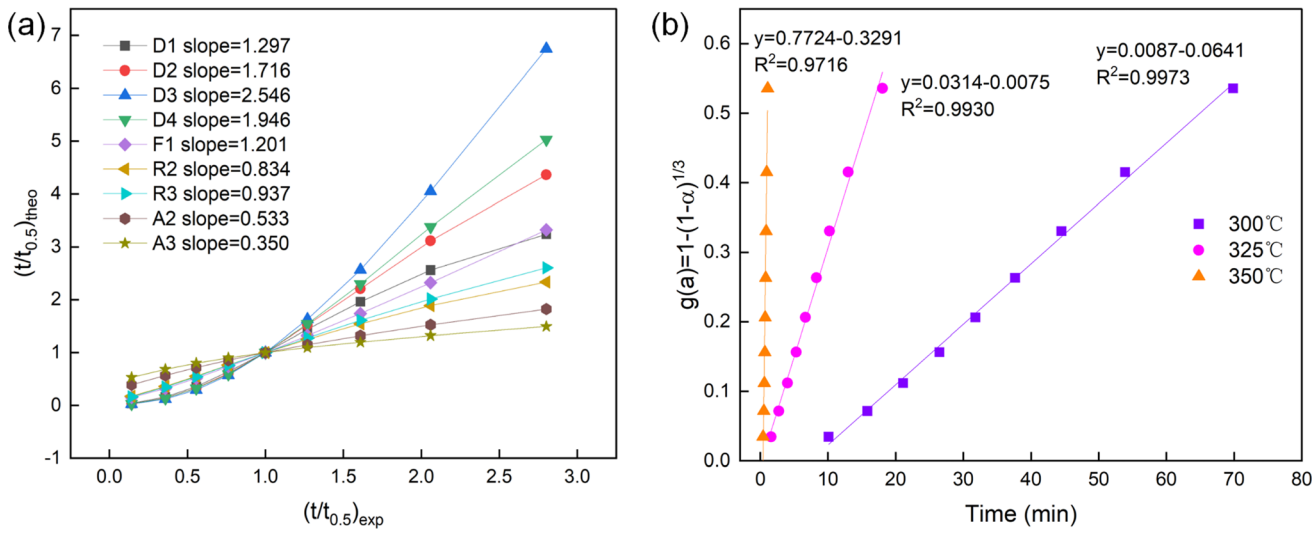

Fig. 4 (a) $(t/t_{0.5})_{theo}$ *vs.* $(t/t_{0.5})_{exp}$ of 10 wt% $BaCrO_4$-modified MgH_2 at 350 °C through fitting different kinetic models. (b) Time dependence of kinetic modeling equations $g(\alpha)$ with $0.1 < \alpha < 0.9$ for 10 wt% $BaCrO_4$-modified MgH_2 at different temperatures.

demonstrates that the R3 model is the most suited kinetic model for the 10 wt% $BaCrO_4$-modified MgH_2 system, which reveals that the hydrogen desorption of 10 wt% $BaCrO_4$-modified MgH_2 is controlled by the three-dimension phase boundary kinetic model. Specifically, the kinetics of hydrogen emission is controlled by the migration of the gas–solid interface towards the center of the nanoparticles.

5.4 Catalytic mechanism of $BaCrO_4$ on MgH_2

To further understand the catalytic mechanism in connection with the hydrogen storage capacity of 10 wt% $BaCrO_4$-modified MgH_2, XRD and TEM were employed aiming to clarify the phase evolution of the MgH_2–$BaCrO_4$ system after ball milling, dehydrogenating and rehydrogenating processes. The XRD patterns are shown in Fig. 5. Owing to the grain refinement during ball milling, the crystallinity and diffraction peak intensity of MgH_2–$BaCrO_4$ are attenuated to some extent.[61] After milling, $BaCrO_4$ could still be detected and there is no MgO generation during this possess, which reflects that there is no obvious oxidation during the preparation process. For the system after dehydrogenation, MgH_2 is fully transformed into Mg, and $BaCrO_4$ still remains without any changes. The diffraction peaks of MgH_2 are found again in the hydrogen release process, which reflects the reversible phase conversion process among the Mg and MgH_2 phases.

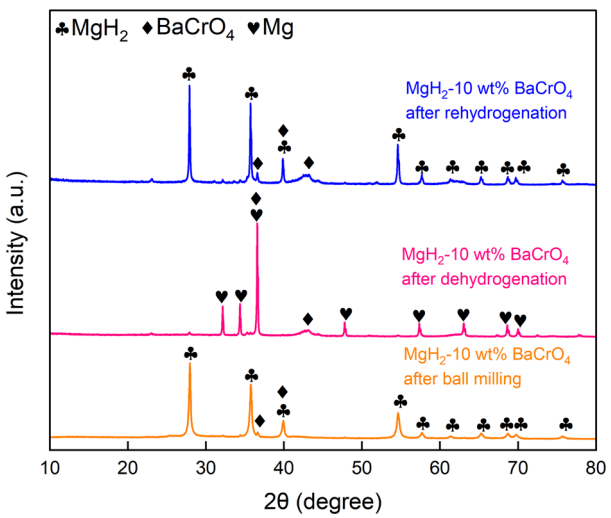

Fig. 5 XRD patterns of 10 wt% $BaCrO_4$-modified MgH_2 at different processes.

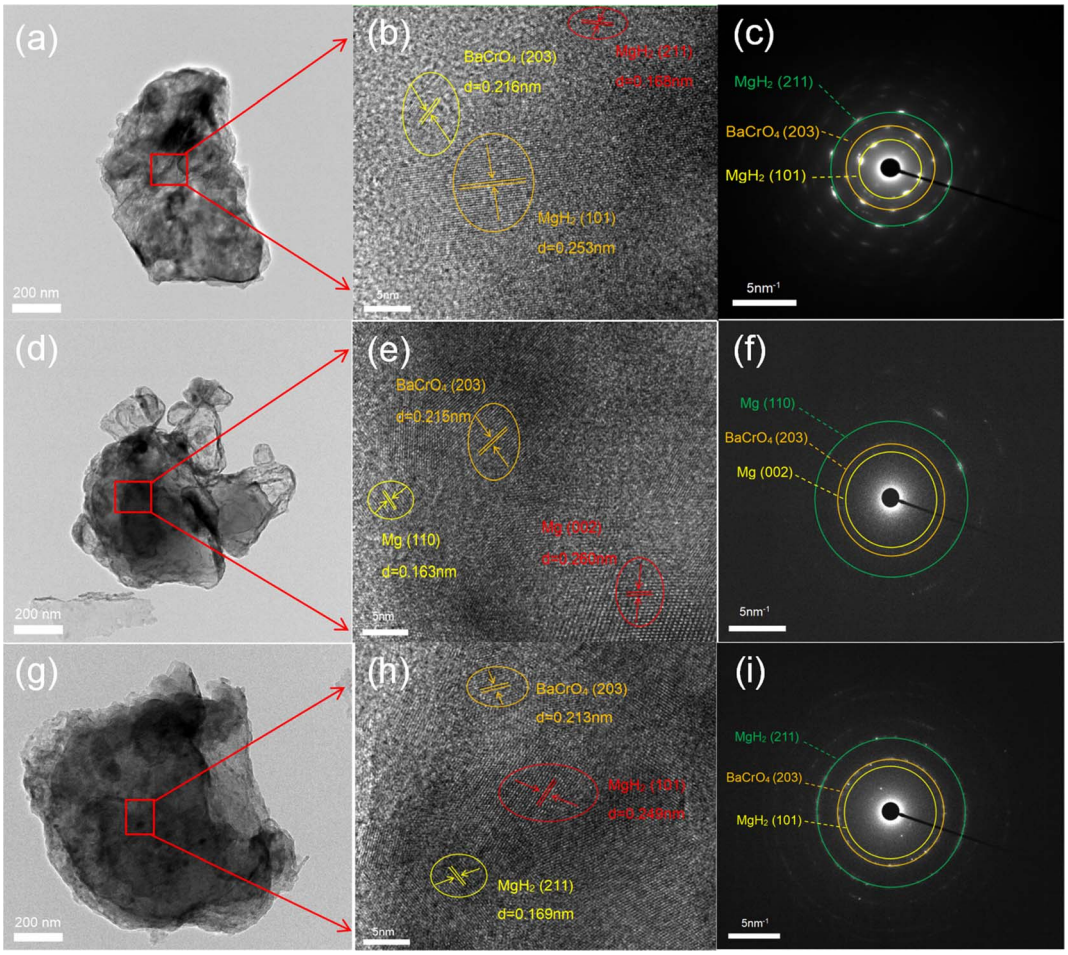

Fig. 6 TEM, HRTEM and SAED patterns of the 10 wt% $BaCrO_4$-modified MgH_2 sample (a–c) after milling, (d–f) after dehydrogenation and (g–i) after rehydrogenation.

Afterward, the HRTEM images and SAED patterns were acquired to verify the phase and structural evolution, The (203) crystal plane of $BaCrO_4$ and the (211) and (101) crystal planes of MgH_2 after milling state with interplanar crystal spacings of 0.216, 0.168 and 0.253 nm are shown in Fig. 6(a–c), which indicate that the $BaCrO_4$ phase exists stably during the milling possess. As shown in Fig. 6(d–f), three groups with interplanar crystal spacings of 0.211 nm, 0.163 nm and 0.260 nm were detected, corresponding to the (410), Mg (110) and Mg (002) crystal planes of $BaCrO_4$, respectively. Meanwhile, the HRTEM and SAED characterizations of 10 wt% $BaCrO_4$-modified MgH_2 after rehydrogenation are exhibited in Fig. 6(g–i). It is proposed that Mg is transformed into MgH_2. Interplanar crystal spacings of 0.213, 0.169, and 0.249 nm correspond to the (203) plane of $BaCrO_4$, and the (101) and (211) planes of MgH_2, respectively. Moreover, the uniform Cr Ba and O elements distributed on the Mg/MgH_2 system can be detected obviously through the EDS mapping test, as shown in Fig. 7(a–c), which exerts a positive effect on the hydrogen storage capacity of MgH_2.

Aiming to thoroughly investigate the action mechanism of $BaCrO_4$ on the Mg–H bonds, theoretical calculations were performed using DFT (density functional theory). Based on the HRTEM and XRD characterization, we selected the MgH_2 (101) and $BaCrO_4$ (203) crystal planes to successfully construct the $MgH_2/BaCrO_4$ heterojunction optimization model, and the results are shown in Fig. 8. The bond length analysis presented in Table S1† illustrates that with the addition of $BaCrO_4$, the average Mg–H bond length is significantly extended from 1.935 Å to 2.904 Å, which reflects that the $BaCrO_4$ catalyst is favorable for weakening the Mg–H bond strength to ameliorate hydrogen release. To reveal the nature of the Mg–H bond interaction in the 10 wt% $BaCrO_4$-modified MgH_2 optimized model, the density-of-states maps of MgH_2 and 10 wt% $BaCrO_4$-modified MgH_2 were calculated.

As shown in Fig. 9(a and b), the binding energy at 0 is set to the Fermi level, as can be seen from the DOS diagram of MgH_2, and the conduction band is mainly composed of the s orbital of H, and the valence charge is mainly composed of the s and p orbitals of Mg. There is a certain hybridization between the s, p and H s orbitals of Mg at the valence band, indicating that MgH_2 is mainly composed of ionic bonds with a small amount of covalent bonds, which leads to the high thermodynamic property and undesirable dehydrogenation capacity. With the addition of $BaCrO_4$, the electrons of the MgH_2-10 wt% $BaCrO_4$

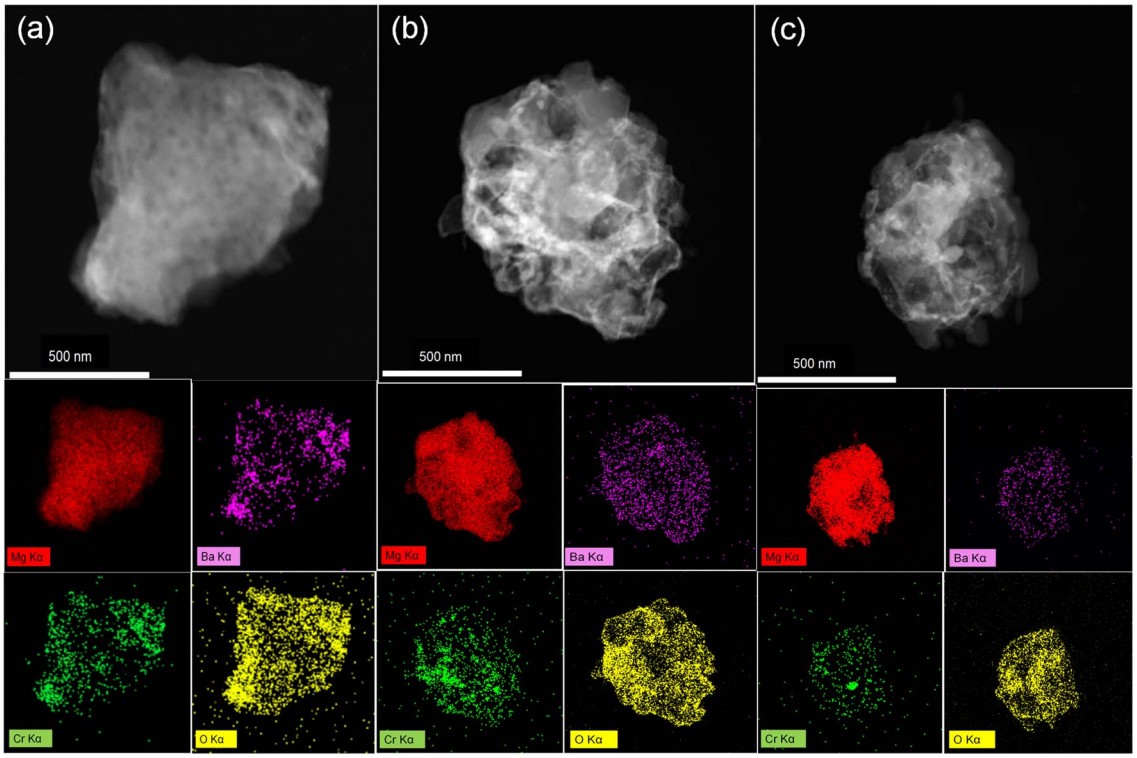

Fig. 7 EDS images of 10 wt% $BaCrO_4$-modified MgH_2 (a) at the milling state, (b) at the dehydrogenation state and (c) after rehydrogenation.

system are mainly contributed by Ba, Cr, and O orbitals. The hybridization between Mg and H in the valence band is weakened, and the band gap decreased from MgH_2 (2.78 eV) to 2.16 eV. This results in a decrease in the stability of the MgH_2 system and an increase in the electron mobility, thereby improving the dehydrogenation performance of MgH_2. Fig. 10 gives the differential charge density maps of 10 wt% $BaCrO_4$-modified MgH_2. It is obvious that the charges around Mg are lacking; in addition to being transferred to H, O will also attract part of the valence charges of Mg, weakening the strong interaction of Mg–H bonds and promoting the fracture of Mg–H bonds and the release of H.

According to the above-mentioned calculation analyses, $BaCrO_4$ ameliorates the thermodynamic capacity *via* weakening the Mg–H bond. However, the kinetics of hydrogen emission in MgH_2 could also affect the hydrogen desorption performance. Specifically, H atoms need to overcome a certain hydrogen release energy barrier from the bond cleavage of Mg–H to the recombination of H molecules. As shown in Fig. 11(a), the transition state (TS) of MgH_2 has a higher dehydrogenation energy barrier of 2.27 eV, and the Mg–H bond energy is still stronger. Interestingly, with the modification of $BaCrO_4$, the dehydrogenation energy barrier of 10 wt% $BaCrO_4$-modified MgH_2 is decreased to 1.54 eV, indicating the significant improvement in the kinetics of hydrogen desorption. These results are consistent with the decreasing trend of activation energy calculated by DSC. The optimized models of 10 wt%

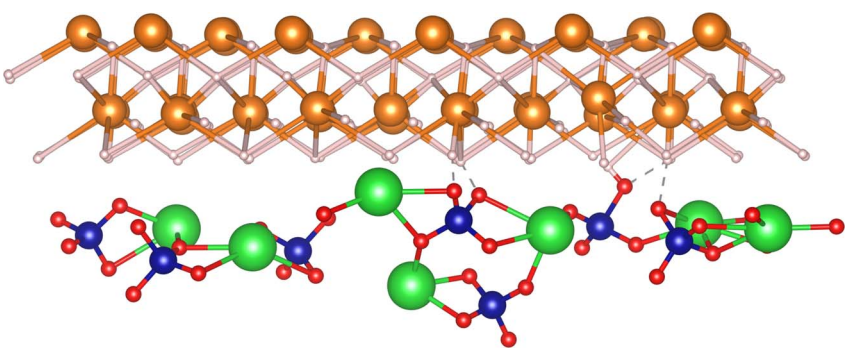

Fig. 8 Optimized structure of the 10 wt% $BaCrO_4$-modified MgH_2 heterojunction (green, blue, red, white and orange represent Ba, Cr, O, H and Mg atoms, respectively).

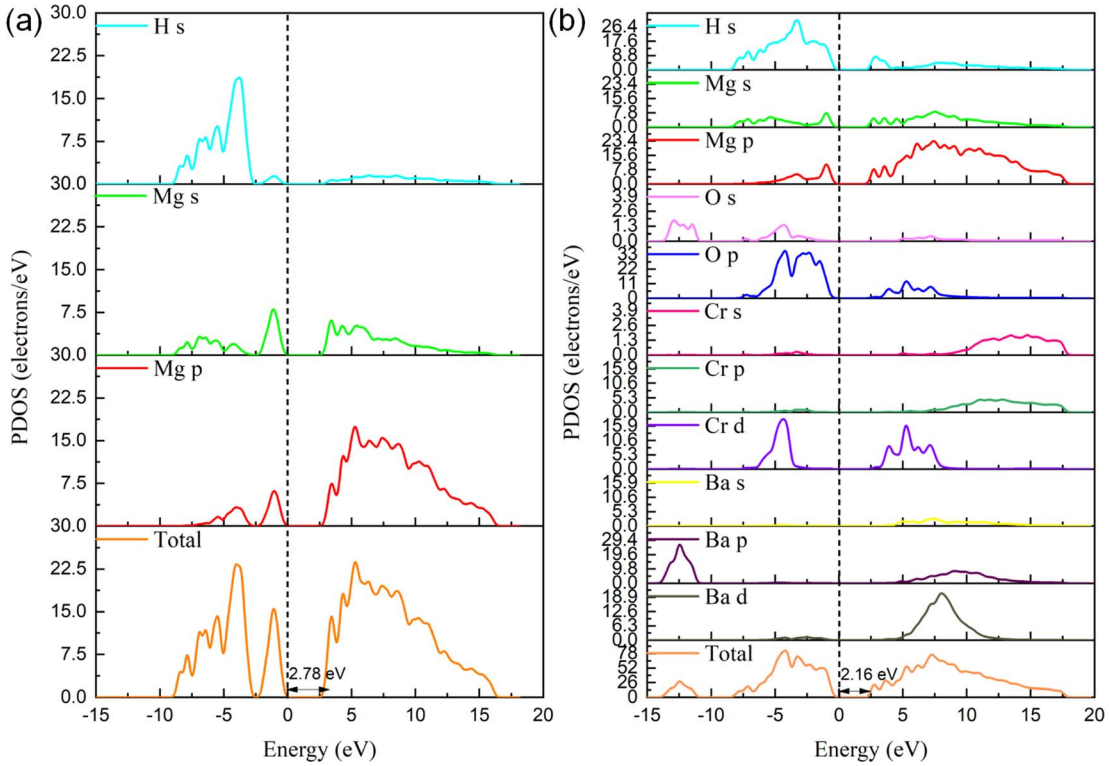

Fig. 9 DOS graphs of (a) MgH_2 and (b) 10 wt% $BaCrO_4$-modified MgH_2.

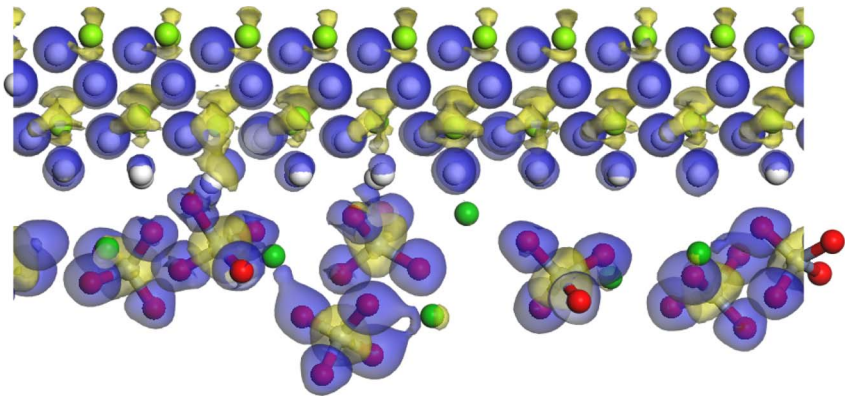

Fig. 10 Differential charge density maps of 10 wt% $BaCrO_4$-modified MgH_2 (blue represents charge stacking and yellow represents charge lacking).

$BaCrO_4$-modified MgH_2 in the initial state (IS), transition state (TS) and final state (FS) are shown in Fig. 11(b–d).

The specific catalytic mechanism of 10 wt% $BaCrO_4$-modified MgH_2 is summarized in Fig. 12. The H atom preferentially diffuses on the $BaCrO_4$ nanocatalyst surface rather than the Mg/MgH_2 surface during hydrogen absorption and desorption periods, because $BaCrO_4$ could shorten the length of the Mg–H bond and reduce the band gap as well as the diffusion energy barrier or E_a, which is shown in the calculation or DSC test section above. The strong electron-withdrawing effect of O and the catalytic effect of Ba and Cr play an important role in improving the kinetic and thermodynamic properties of MgH_2. Meantime, the $BaCrO_4$ nanocatalyst provides a number of sites for nucleation and channels for hydrogen diffusion to ameliorate the hydrogen storage capacity.

Additionally, after refinement of the high-energy ball mill technology, the $BaCrO_4$ nanocatalyst uniformly dispersed on the surface of MgH_2 efficiently prevents aggregation and crystal growth phenomenon, which results in excellent cycling property.

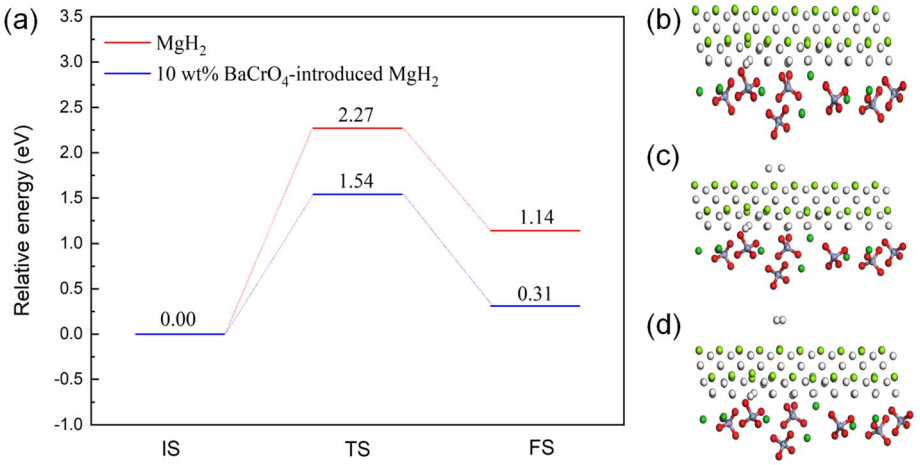

Fig. 11 (a) Dehydrogenation barrier energy of MgH_2 and 10 wt% $BaCrO_4$-modified MgH_2. (b–d) IS, TS, FS states of 10 wt% $BaCrO_4$-modified MgH_2.

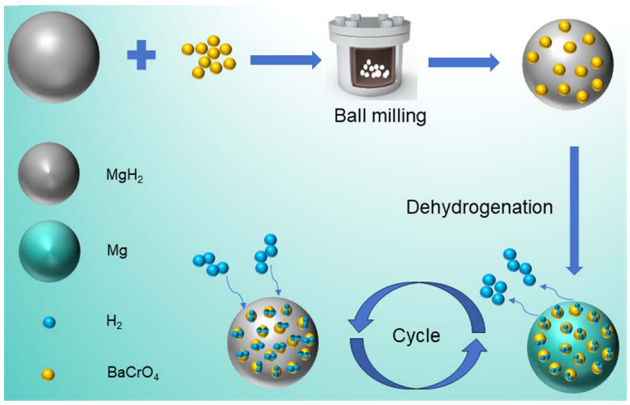

Fig. 12 Schematic catalytic mechanism of MgH_2 added with $BaCrO_4$.

6 Conclusions

In this work, we have successfully fabricated a $BaCrO_4$ nanocatalyst *via* wet chemical technology and introduced it into MgH_2 to study the catalytic effect in detail. The T_{onset} value of MgH_2 modified with 10 wt% $BaCrO_4$ was decreased to 280 °C, which is in sharp contrast to milled MgH_2 (390 °C). The 10 wt% $BaCrO_4$-modified MgH_2 sample could fully absorb 5.78 wt% H_2 within 10 min at 300 °C. and release 4.25 wt% H_2 in 10 min at 325 °C, which is higher than that of undoped MgH_2 that adsorbed 1.25 wt% H_2 and desorbed 0.15 wt% H_2 during the same period. The desorption E_a value decreased from 156.55 kJ mol^{-1} to 106.75 kJ mol^{-1}. Notably, the results of the cycle dynamic test indicated that $BaCrO_4$-modified MgH_2 could store 5.95 wt% H_2 after 10 cycles, with a 95% volume retention rate. The DFT calculations illustrated that $BaCrO_4$ could shorten the length of Mg–H bonds and reduce the band gap from 2.78 eV (milled MgH_2) to 2.16 eV, thereby improving the thermodynamic property. Impressively, the dehydrogenation energy barrier decreased from 2.27 eV (milled MgH_2) to 1.54 eV owing to the $BaCrO_4$ nanocatalyst. In conclusion, the above-mentioned results reveal that $BaCrO_4$ is an ideal modified material to ameliorate the kinetics and thermodynamics of MgH_2, which could contribute to the strong electron-withdrawing effect of oxygen atoms and the catalytic effect of Ba and Cr elements.

Data availability

Data will be made available on request.

Conflicts of interest

The authors declare that they have no conflict of interest.

Acknowledgements

This work was financially supported by Applied Basic Research Project of Qinghai province (2022-ZJ-769).

References

1 C. Tarhan and M. A. Cil, *J. Energy Storage*, 2021, **40**, 102676–102686.
2 Z.-Y. Li, Y.-J. Sun, C.-C. Zhang, S. Wei, L. Zhao, J.-L. Zeng, Z. Cao, Y.-J. Zou, H.-L. Chu, F. Xu, L.-X. Sun and H.-G. Pan, *J. Mater. Sci. Technol.*, 2023, **141**, 221–235.
3 S. Dutt, A. Singh, R. Mahadeva, A. K. Sundramoorthy, V. Gupta and S. Arya, *Diamond Relat. Mater.*, 2024, **141**, 110554.
4 M. Thakur, A. Singh, A. Dubey, A. K. Sundramoorthy, P. Kumar and S. Arya, *Emergent Mater.*, 2024, DOI: 10.1007/s42247-024-00729-7.
5 P. Murugan, A. K. Sundramoorthy, R. D. Nagarajan, R. Atchudan, R. Shanmugam, D. Ganapathy, S. Arya, A. A. Alothman and M. Ouladsmane, *J. Nanomater.*, 2022, **2022**, 9866111–9866121.
6 H. Ishaq, I. Dincer and C. Crawford, *Int. J. Hydrogen Energy*, 2022, **47**, 26238–26264.

7 T. R. Somo, T. E. Mabokela, D. M. Teffu, T. K. Sekgobela, M. J. Hato and K. D. Modibane, *Chem. Pap.*, 2021, **75**, 2237–2251.
8 Z. Taie, G. Villaverde, J. Speaks Morris, Z. Lavrich, A. Chittum, K. White and C. Hagen, *Int. J. Hydrogen Energy*, 2021, **46**, 3365–3378.
9 J. J. Brey, *Int. J. Hydrogen Energy*, 2021, **46**, 17447–17457.
10 R. Kumar Mishra, G. Jin Choi, R. Verma, S. Hun Jin, R. Bhardwaj, S. Arya, J. Singh and J. Seog Gwag, *Mater. Sci. Eng., B*, 2024, **303**, 117292.
11 J. Q. Li, J. C. Li, K. Park and J. T. Kwon, *Case Stud. Therm. Eng.*, 2022, **37**, 102143–102155.
12 K. E. Lamb and C. J. Webb, *J. Alloys Compd.*, 2022, **906**, 164235–164245.
13 L. Jiang, *Engineering*, 2021, **7**, 731–733.
14 H. Zhong, H. Wang, J. W. Liu, D. L. Sun, F. Fang, Q. A. Zhang, L. Z. Ouyang and M. Zhu, *J. Alloys Compd.*, 2016, **680**, 419–426.
15 Y. Zhang, X. Wei, W. Zhang, Z. Yuan, J. Gao, Y. Qi and H. Ren, *Int. J. Hydrogen Energy*, 2020, **45**, 33832–33845.
16 X. Chen, H. Yang and F. Pan, *J. Magnesium Alloys*, 2021, **9**, 1835–1836.
17 Q. Li, Y. Lu, Q. Luo, X. Yang, Y. Yang, J. Tan, Z. Dong, J. Dang, J. Li, Y. Chen, B. Jiang, S. Sun and F. Pan, *J. Magnesium Alloys*, 2021, **9**, 1922–1941.
18 N. Patelli, A. Migliori, V. Morandi and L. Pasquini, *Nano Energy*, 2020, **72**, 104654–104664.
19 C. Duan, Y. Tian, X. Wang, M. Wu, D. Fu, Y. Zhang, W. Lv, Z. Su, Z. Xue and Y. Wu, *Renewable Energy*, 2022, **187**, 417–427.
20 X. Zhang, Y. Liu, Z. Ren, X. Zhang, J. Hu, Z. Huang, Y. Lu, M. Gao and H. Pan, *Energy Environ. Sci.*, 2021, **14**, 2302–2313.
21 Z. Y. Lu, H. J. Yu, X. Lu, M. C. Song, F. Y. Wu, J. G. Zheng, Z. F. Yuan and L. T. Zhang, *Rare Met.*, 2021, **40**, 3195–3205.
22 P. Vajeeston, P. Ravindran, M. Fichtner and H. Fjellvåg, *J. Phys. Chem. C*, 2012, **116**, 18965–18972.
23 Z. Ma, Q. Zhang, S. Panda, W. Zhu, F. Sun, D. Khan, J. Dong, W. Ding and J. Zou, *Sustainable Energy Fuels*, 2020, **4**, 4694–4703.
24 Z. Ma, S. Panda, Q. Zhang, F. Sun, D. Khan, W. Ding and J. Zou, *Chem. Eng. J.*, 2021, **406**, 126790–126800.
25 A. Singh, S. S. Shah, C. Sharma, V. Gupta, A. K. Sundramoorthy, P. Kumar and S. Arya, *J. Environ. Chem. Eng.*, 2024, **12**, 113032.
26 H. Yong, X. Wei, J. Hu, Z. Yuan, M. Wu, D. Zhao and Y. Zhang, *Renewable Energy*, 2020, **162**, 2153–2165.
27 X. Chen, J. Zou, X. Zeng and W. Ding, *Int. J. Hydrogen Energy*, 2016, **41**, 14795–14806.
28 X. Wei, W. Zhang, H. Sun, Z. Yuan, Q. Ge, Y. Zhang and Y. Qi, *Int. J. Hydrogen Energy*, 2022, **47**, 12653–12664.
29 S. Balu, D. Ganapathy, S. Arya, R. Atchudan and A. K. Sundramoorthy, *RSC Adv.*, 2024, **14**, 14392–14424.
30 K. Kajiwara, H. Sugime, S. Noda and N. Hanada, *J. Alloys Compd.*, 2022, **893**, 162206–162213.
31 P. Yao, Y. Jiang, Y. Liu, C. Wu, K.-C. Chou, T. Lyu and Q. Li, *J. Magnesium Alloys*, 2020, **8**, 461–471.
32 F. J. Antiqueira, D. R. Leiva, G. Zepon, B. F. R. F. de Cunha, S. J. A. Figueroa and W. J. Botta, *Int. J. Hydrogen Energy*, 2020, **45**, 12408–12418.
33 H. C. S. Perera, V. Gurunanthanan, A. Singh, M. M. M. G. P. G. Mantilaka, G. Das and S. Arya, *J. Magnesium Alloys*, 2024, **12**, 1709–1773.
34 R. Schulz, J. Huot, G. Liang, S. Boily, G. Lalande, M. C. Denis and J. P. Dodelet, *Mater. Sci. Eng., A*, 1999, **267**, 240–245.
35 R. A. Varin, T. Czujko and Z. Wronski, *Nanotechnology*, 2006, **17**, 3856–3865.
36 X. Yang, J. Zhang, Q. Hou, X. Guo and G. Xu, *ChemistrySelect*, 2021, **6**, 8809–8829.
37 D. Pukazhselvan, K. S. Sandhya, D. Ramasamy, A. Shaula and D. P. Fagg, *ChemPhysChem*, 2020, **21**, 1195–1201.
38 P. Rizo-Acosta, F. Cuevas and M. Latroche, *J. Mater. Chem. A*, 2019, **7**, 23064–23076.
39 Y. Huang, C. An, Q. Zhang, L. Zang, H. Shao, Y. Liu, Y. Zhang, H. Yuan, C. Wang and Y. Wang, *Nano Energy*, 2021, **80**, 105535–105545.
40 V. N. Kudiiarov, N. Kurdyumov, R. R. Elman, R. S. Laptev, M. A. Kruglyakov, I. A. Ushakov, A. V. Tereshchenko and A. M. Lider, *J. Alloys Compd.*, 2023, **966**, 171534–171548.
41 N. A. Sazelee, N. H. Idris, M. F. Md Din, N. S. Mustafa, N. A. Ali, M. S. Yahya, F. A. Halim Yap, N. N. Sulaiman and M. Ismail, *Int. J. Hydrogen Energy*, 2018, **43**, 20853–20860.
42 J. Adedeji Bolarin, Z. Zhang, H. Cao, Z. Li, T. He and P. Chen, *J. Phys. Chem. C*, 2021, **125**, 19631–19641.
43 N. A. Sazelee, N. A. Ali, M. S. Yahya, M. F. M. Din and M. Ismail, *Int. J. Hydrogen Energy*, 2023, **48**, 30844–30857.
44 N. A. Sazelee, N. H. Idris, M. F. Md Din, M. S. Yahya, N. A. Ali and M. Ismail, *Results Phys.*, 2020, **16**, 102844–102851.
45 S. Zhou, D. Wei, H. Wan, X. Yang, Y. Dai, Y. a. Chen and F. Pan, *Inorg. Chem. Front.*, 2022, **9**, 5495–5506.
46 M. H. Abdul Rahman, M. A. Shamsudin, A. Klimkowicz, S. Uematsu and A. Takasaki, *Int. J. Hydrogen Energy*, 2019, **44**, 29196–29202.
47 N. Sazelee, M. F. Md Din, M. Ismail, S.-U. Rather, H. S. Bamufleh, H. Alhumade, A. A. Taimoor and U. Saeed, *Materials*, 2023, **16**(6), 2449–2463.
48 H. Gao, R. Shi, Y. Shao, Y. Liu, Y. Zhu, J. Zhang and L. Li, *Int. J. Hydrogen Energy*, 2022, **47**, 9346–9356.
49 Y. Fu, L. Zhang, Y. Li, S. Guo, Z. Yu, W. Wang, K. Ren, Q. Peng and S. Han, *J. Mater. Sci. Technol.*, 2023, **138**, 59–69.
50 R. Kesarwani, A. Bhatnagar, S. K. Verma, M. S. L. Hudson and M. A. Shaz, *Int. J. Hydrogen Energy*, 2024, **67**, 1026–1032.
51 Y. Cheng, W. Zhang, J. Chen, J. Wang, P. Pei and F. Li, *RSC Adv.*, 2023, **13**, 9091–9098.
52 H. E. Kissinger, *Anal. Chem.*, 1957, **29**, 1702–1706.
53 N. H. Idris, N. S. Mustafa and M. Ismail, *Int. J. Hydrogen Energy*, 2017, **42**, 21114–21120.
54 S. Hu, H. Zhang, Z. Yuan, Y. Wang, G. Fan, Y. Fan and B. Liu, *J. Alloys Compd.*, 2021, **881**, 160571–160579.
55 M. S. Yahya and M. Ismail, *J. Energy Chem.*, 2019, **28**, 46–53.
56 L. Dan, L. Hu, H. Wang and M. Zhu, *Int. J. Hydrogen Energy*, 2019, **44**, 29249–29254.
57 F. A. Halim Yap, N. N. Sulaiman and M. Ismail, *Int. J. Hydrogen Energy*, 2019, **44**, 30583–30590.

58 N. A. Ali, N. A. Sazelee, M. F. Md Din, M. M. Nasef, A. A. Jalil, H. Liu and M. Ismail, *J. Magnesium Alloys*, 2023, **11**, 2205–2215.
59 J. H. Sharp, G. W. Brindley and B. N. N. Achar, *J. Am. Ceram. Soc.*, 1966, **49**, 379–382.
60 L. F. Jones, D. Dollimore and T. Nicklin, *Thermochim. Acta*, 1975, **13**, 240–245.
61 H. Wan, X. An, Q. Kong, X. Wu, W. Feng, H. Wang, J. Wu, C. Lu, W. Zha, H. Sun and L. Huang, *Adv. Powder Technol.*, 2021, **32**, 1380–1389.